Tunable plasmonic bound states in the continuum in the visible range

Shuoyan Sun,[1,*] Yufeng Ding,[1,*] Haozhi Li,[1] Peng Hu,[2] Chang-Wei Cheng,[3] Yungang Sang,[1,3] Fengzhao Cao,[1] Yue Hu,[1] Andrea Alù,[4] Dahe Liu,[1] Zhaona Wang,[1] Shangjr Gwo,[3,5,†] Dezhuan Han,[2,‡] and Jinwei Shi[1,§]

[1]*Department of Physics and Applied Optics Beijing Area Major Laboratory, Beijing Normal University, Beijing 100875, People's Republic of China*

[2]*College of Physics, Chongqing University, Chongqing 401331, People's Republic of China*

[3]*Department of Physics, National Tsing-Hua University, Hsinchu 30013, Taiwan*

[4]*Photonics Initiative, Advanced Science Research Center, City University of New York, New York, New York 10031, USA*

[5]*Research Center for Applied Sciences, Academia Sinica, Nankang, Taipei 11529, Taiwan*

(Received 3 August 2020; revised 24 November 2020; accepted 17 December 2020; published 15 January 2021)

Bound states in the continuum (BICs) have been observed in a variety of systems. A plasmonic BIC offers interesting opportunities, since a surface plasmon is known to confine light to the nanometer scale. However, the observation and manipulation of plasmonic BICs is a challenge due to the intrinsic loss of metals. Here, we study plasmonic BICs in the visible range in a one-dimensional all-metallic grating. First, by tuning the resonances of localized and propagating surface plasmon modes to resonance, we successfully observe symmetry-protected plasmonic BICs in an all-metallic system. Next, by continuously tuning the localized mode, we demonstrate topological band inversion characterized by a Zak phase transition. In addition, we engineer off-Γ-point BICs and confirm their formation mechanism. Finally, we experimentally determine that the quality (Q) factor of a 10-groove structure can exceed 60, about one order of magnitude greater than conventional metallic structures. The simulations reveal that, with more grooves, the Q factor can be over 200. The plasmonic BICs in the visible range demonstrated in this paper pave the way to promising applications in lasers, sensors, light-matter interactions, nonlinear optics, and quantum optics.

DOI: 10.1103/PhysRevB.103.045416

I. INTRODUCTION

In 1929, von Neumann and Wigner proposed the concept of a "bound state in the continuum" (BIC) when studying the single-particle Schrödinger equation [1]. A BIC can support a perfectly confined state, even above the continuum threshold. In theory, a BIC, also known as an embedded eigenstate [1], manifests itself as a resonance with an infinite radiative quality factor and a zero linewidth. The initial concept was a somewhat artificial proposal which has never been observed in quantum mechanics. Since then, various formation mechanisms of BICs have been studied. In 1985, Friedrich and Wintgen derived the equation of a special type of BIC (named after them), which is due to the destructive interference of two resonances coupled to the same radiation channel [2]. As a wave phenomenon, BICs can be found in different areas of wave physics, including acoustics, microwaves, and photonics [3–14]. BICs in photonic systems have been realized in one-dimensional (1D) arrays of coupled waveguides [9,15], dielectric spheres [16,17], disks [18,19], and two-dimensional (2D) photonic crystals (PCs) [20–22]. On the other hand, surface plasmon polaritons (SPPs) have been observed in many applications during the past few decades, due to their ability to confine the optical field to the nanometer scale [22–25]. However, the design and manipulation of BICs in an all-plasmonic system have yet to be reported. Due to its intrinsic loss, the observation of a plasmonic BIC is a challenge [26], and metallic structures that support plasmonic BICs have remained limited [27–29]. In particular, a plasmonic BIC in the visible range has not been reported. Strong coupling in all plasmonic systems has been previously reported [30,31] but has never been used to study BIC.

In this paper, using more than 20 samples, we systematically studied plasmonic BICs in the visible range by harnessing the strong coupling between localized surface plasmon resonant (LSPR) modes and lattice SPPs (LSPPs). Due to intrinsic loss, the effective interaction length between different modes is finite; therefore, a plasmonic BIC is always a quasi-BIC. First, by tuning the LSPRs and LSPPs to be completely on resonance, we successfully observed symmetry-protected plasmonic quasi-BICs (Type I BIC) in an all-metallic system. Next, by continuously tuning LSPRs, we observed a topological band inversion corresponding to the "vanishing" of a BIC, which, to our knowledge, has never been reported in plasmonic crystals. The bandgap at the center of the Brillouin zone (Γ point) is closed, resulting in a 1D Dirac point, which is then opened again. This topologic band inversion can be characterized by a Zak phase transition. In addition, we also implemented nontrivial off-Γ-point quasi-BICs (Type II BICs) and explained their formation mechanism. Previously, this type of off-Γ-point BIC in other systems was referred to as an "accidental BIC" [11]. Finally, we also measured the

*S.S. and Y.D. contributed equally to this paper.
†gwo@phys.nthu.edu.tw
‡dzhan@cqu.edu.cn
§shijinwei@bnu.edu.cn

Q factors of samples with various parameters. Although each sample was composed of only 10 grooves, so lattice effects are expected to be quite limited, the typical Q factor can exceed 60, which is considerably larger than that in typical metallic structures (<10). The simulations reveal that, with more grooves, the Q factor can even be increased to over 200. The observation and manipulation of plasmonic quasi-BICs open a route for obtaining a high Q plasmonic cavity, which may find applications in high-sensitivity sensors, low-threshold lasers, nonlinear frequency conversion, light-matter interactions, and quantum information [32–45].

II. THEORY FOR MULTIMODE COUPLING

We start from the well-known band structure of a two-coupled-mode PC with finite size. Based on coupled mode theory (CMT), the Hamiltonian is

$$H = \begin{pmatrix} \frac{E_i - i\gamma_i}{2} & g_{\mathrm{bg}} \\ g_{\mathrm{bg}} & \frac{E_j - i\gamma_j}{2} \end{pmatrix}, \tag{1}$$

where E_i and E_j are two propagating plasmonic modes, $\gamma_i = \gamma_j = \gamma$ are the decay rates of the modes due to absorption, and g_{bg} denotes the coupling strength between these two modes. In this expression, due to symmetry, the original modes are identical, except for the direction of the wave vectors. If we only consider the Γ point ($E_i = E_j$), then the eigenvalues are simply given by

$$E_- \equiv E_a = E_i - g_{\mathrm{bg}} - \frac{i\gamma}{2}, \tag{2a}$$

$$E_+ \equiv E_b = E_i + g_{\mathrm{bg}} - \frac{i\gamma}{2}, \tag{2b}$$

for the corresponding eigenstates (as an approximation, ignoring $\gamma/2$):

$$\psi_- = \frac{\sqrt{2}}{2}\begin{pmatrix} 1 \\ -1 \end{pmatrix}, \tag{3a}$$

$$\psi_+ = \frac{\sqrt{2}}{2}\begin{pmatrix} 1 \\ 1 \end{pmatrix}. \tag{3b}$$

These general results apply to both photonic and plasmonic structures. From Eq. (3a), we can see that the zero-detuning point of the lower eigenstate is a BIC, which is referred to as a symmetry-protected BIC. A typical example is a one-layer PC, the dielectric grating. According to convention, this state is defined as a Type I BIC in the following discussions. These results are well established for low-loss PCs, where the bandgap equals twice the coupling strength g_{bg}. However, for plasmonic crystals (e.g., metallic gratings), due to the larger Ohmic loss of metals ($\gamma \gg g_{\mathrm{bg}}$), the quasi-BIC is usually hidden by the bright upper mode [Eq. (3b)] on the other side of the small bandgap, making it difficult to observe. Note that, for this one-layer PC, state ψ_+ can strongly couple to the far field, which will add an extra radiation decay γ_{rad} and hence a broader linewidth than in Eq. (2b).

To circumvent this problem, we consider a three-coupled-mode plasmonic crystal containing two LSPP modes and one LSPR mode:

$$H = \begin{pmatrix} E_{\mathrm{LSPR}} - \frac{i\gamma_{\mathrm{LSPR}}}{2} & g_{\mathrm{str}} & g_{\mathrm{str}} \\ g_{\mathrm{str}} & E_i - \frac{i\gamma_i}{2} & g_{\mathrm{bg}} \\ g_{\mathrm{str}} & g_{\mathrm{bg}} & E_j - \frac{i\gamma_j}{2} \end{pmatrix}, \tag{4}$$

where g_{bg} is again the coupling strength between LSPP modes, and g_{str} represents the coupling between LSPR and LSPP modes. The full expression becomes more complex, but if we operate at the Γ point and assume that all plasmonic decay rates are the same, i.e., $\gamma_{\mathrm{LSPR}} = \gamma_i = \gamma_j = \gamma$, the eigenvalues can be written as

$$E_a = E_i - g_{\mathrm{bg}} - \frac{i\gamma}{2}, \tag{5a}$$

$$E_b = \frac{E_{\mathrm{LSPR}} + E_i + g_{\mathrm{bg}} + \sqrt{(E_{\mathrm{LSPR}} - E_i - g_{\mathrm{bg}})^2 + 8{g_{\mathrm{str}}}^2}}{2} - \frac{i\gamma}{2}, \tag{5b}$$

$$E_c = \frac{E_{\mathrm{LSPR}} + E_i + g_{\mathrm{bg}} - \sqrt{(E_{\mathrm{LSPR}} - E_i - g_{\mathrm{bg}})^2 + 8{g_{\mathrm{str}}}^2}}{2} - \frac{i\gamma}{2}. \tag{5c}$$

The eigenstate corresponding to Eq. (5a) is (as an approximation, ignoring $\gamma/2$)

$$\psi_a = \frac{\sqrt{2}}{2}\begin{pmatrix} 0 \\ 1 \\ -1 \end{pmatrix}, \tag{6}$$

which still supports a quasi-BIC.

From Eq. (5a), we see that the BIC point remains unchanged even in the presence of a third mode. This behavior can be understood because a BIC is inherently nonradiative; hence, it can neither be excited directly from, nor radiate to, the far field. However, different from Eq. (2), the bandgap at the Γ point is

$$\Omega = E_b - E_c = \sqrt{(E_{\mathrm{LSPR}} - E_i - g_{\mathrm{bg}})^2 + 8{g_{\mathrm{str}}}^2}, \tag{7}$$

which can be tuned by the coupling strength g_{str} and the detuning of the LSPR with respect to LSPP. The minimum value of Ω is equal to the Rabi splitting of the strongly coupled system $\sim 2\sqrt{2}g_{\mathrm{str}}$. In other words, the bright upper mode [Eq. (2b)] is now split into two bands and pushed away from the Type I BIC, making it easier to observe it. Notice again that an extra radiation decay γ_{rad} should be added to Eqs. (5b) and (5c). These results are summarized in Fig. 1.

When more than one LSPR mode is involved in strong coupling, even at the Γ point, the results become more complicated. However, one can always prove that Eq. (5a) is a solution to the system. An example of a four-coupled-mode system can be found in Eq. (S1) (see the Supplemental Material [46]). Therefore, in any metallic grating, if the Rabi splitting is larger than the linewidth of the plasmonic mode, a Type I BIC can always be observed by careful mode tuning.

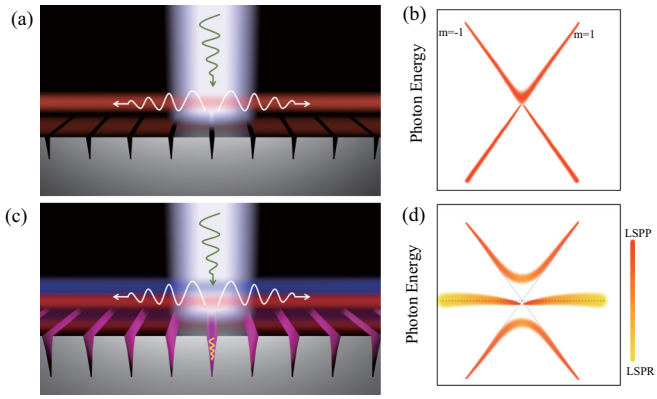

FIG. 1. Illustration of Type I bound states in the continuum (BICs) in an all-plasmonic system. (a) and (b) Without strong coupling, only one mode is bright at the Γ point, hindering the observation of the dark mode (BIC) in the visible range. (c) and (d) With the addition of the localized surface plasmon resonant (LSPR), the single bright mode is split into two modes, making the dark BIC uncovered.

III. EXPERIMENTAL RESULTS

To demonstrate this theory, we fabricated tens of samples with different groove depths. Single-crystalline Ag plates were synthesized using platinum (Pt)-nanoparticle-catalysed and ammonium hydroxide (NH_4OH)-controlled polyol reduction methods [47]. The Ag plates were drop-cast over an indium tin oxide (ITO)-coated glass substrate for subsequent nanofabrication. The V-shaped nanogrooves (gratings) were milled by using an focused ion beam (FIB) lithography system (FEI Nova Nanolab 200, 30-kV acceleration voltage, 10-pA ion beam current, and FEI Helios Nanolab 600i, 30-kV acceleration voltage, 7.7-pA ion beam current). The FIB-fabricated samples were then immediately coated with 5 nm-thick Al_2O_3 through atomic layer deposition (ALD) to avoid the degradation of the silver plates in the ambient environment. The key parameter to introduce and control the third mode is the groove depth, since it determines the LSPR photon energy. The angle-resolved reflection spectra were then collected by a homemade angle-resolved spectrometer [Fig. 2(a)]. We used halogen lamps (HL-2000-CAL, Ocean Optics, Inc.) as the light source. The polarization of the incident light was controlled by a linear polarizer and was perpendicular to the grating. Finally, the Fourier plane of the diffraction light is projected on the entrance slit of a spectrometer with a 2D charge-coupled device (CCD). A CCD (DU970P-BVF, Andor) and spectrometer (Omni-λ 500, Zolix) were used to collect the back focal plane (Fourier plane) signal. The experimentally measured data were [λ, $\sin(\theta)$], which were converted to EN and $k_{//}$ using the formulas $k_{//} = 2\pi \times \sin(\theta)/\lambda$ and $\mathrm{EN} = hc/\lambda$, where EN represents the photon energy. The results from five typical samples are shown in Fig. 3. We can see that, whenever an LSPR is close to the crossing point of two LSPP modes, there is a "breaking" point (high-reflectivity point) in the hybrid band, as marked by black-dashed ellipses. Since this is a far-field measurement, a breaking point is one distinct feature of the BIC formation (another distinct feature is the quality factor, which will be discussed later). The Type I BIC can be seen more clearly with decreasing detuning between the LSPR and LSPP [Figs. 3(a)–3(e)], which is finally completely isolated from the broad linewidth of the bright mode, showing the ability to tune the plasmonic BIC with strong coupling. The dark- and bright-field images on top of each spectrum show the variation of sample color due to the tuning of strong coupling between LSPR and LSPP, although the pitch is fixed.

Based on multimode CMT, we could fit the results using $g_{\mathrm{bg}} = 0.02\,\mathrm{eV}$ and $g_{\mathrm{str}} = 0.15\,\mathrm{eV}$, as shown in Fig. S2 (see the

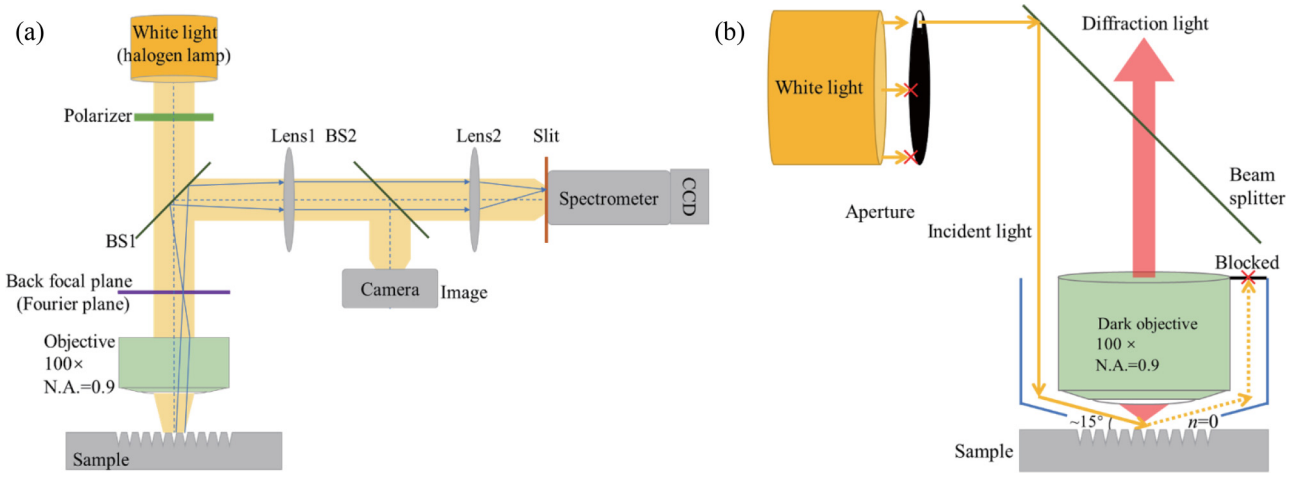

FIG. 2. Experimental optical path diagram. (a) Schematic of the optical setup of angle-resolved spectroscopy. A white light beam (halogen lamp) was projected on the sample by a microscope objective (Olympus,100 ×, NA = 0.9). Parallel light reflected from the sample was focused at the back focal plane (Fourier plane) of the objective and a lens assembly (Lens1 and Lens2) was used to project the Fourier plane onto the entrance slit of a spectrometer. An image of the sample was project on the camera after Lens1 and BS2. BS: beam splitter, Lens: tube lens. (b) Schematic of the optical setup of diffractive angle-resolved spectroscopy. Here, we only show the incident part; the other part is the same as (a). White light is incident on the sample with a very large incident angle using a dark-field objective. The diffractive light is collected by the objective and sent to the angle-resolved spectrometer.

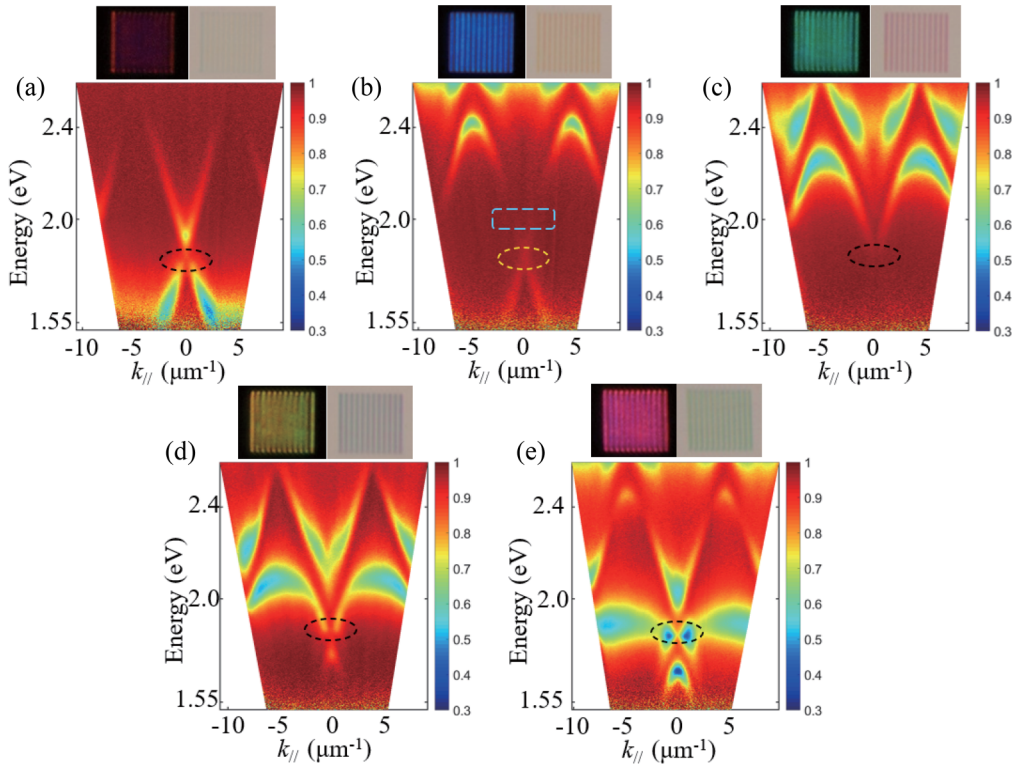

FIG. 3. Angle-resolved reflection spectra of a one-dimensional (1D) silver grating with a fixed pitch (670 nm) with different groove depths of 335, 411, 446, 501, and 550 nm. (a)–(e) The two localized surface plasmon resonant (LSPR) modes are tuned from blue to red by increasing the groove depth. The black-dashed ellipses mark the positions of the Type I bound state in the continuum (BIC). The yellow ellipse denotes the 1D Dirac point, which will be discussed in Fig. 5. The blue rectangle represents the Type II BICs, which will be discussed in Fig. 6. The top of each spectrum shows the dark-field and bright-field images of the corresponding grating. The size of each grating is ∼10 μm. The fitting curves based on CMT can be found in Fig. S2, which indicates that $g_{\mathrm{bg}} = 0.02$ eV and $g_{\mathrm{str}} = 0.15$ eV.

Supplemental Material [46]). We used the finite-difference-time-domain method to calculate the angle-resolved reflection spectrum, and the simulated reflectivity is shown in Fig. 4. The pitch is the same as in the experiment 670 nm. The groove depth varied from 180 to 270 nm. The substrate material was silver (Palik, 0–2 μm). We set the light source as a plane wave, and the polarization of the incident light was perpendicular to the grating. The angle scanning range was from $-30\,^\circ$ to $+30\,^\circ$. The wavelength range was from 400 to 800 nm, and the obtained data were partially intercepted. Type I BICs are also marked by black-dashed ellipses. Both theoretical results and simulations are consistent with the experimental results, validating our analysis.

IV. TOPOLOGICAL PROPERTY OF THE BAND

Next, we studied topological band inversion in this system. In Fig. 3, by continuously tuning the LSPR resonance, we observe that the hybrid bandgap Γ point is closed and opened again. When closed, a 1D Dirac point arises [marked by a yellow ellipse in Fig. 3(b)], corresponding to the vanishing of the Type I BIC. Since at least two LSPR modes are involved here, we considered the simplified four-mode system in Eq. (S1). When Eq. (S3) is satisfied, two of the four eigenvalues are equal:

$$E_b = E_a = E_i - g_{\mathrm{bg}} - \frac{i\gamma}{2}, \tag{8}$$

leading to the generation of a plasmonic 1D Dirac point. Since the bright mode and quasi-BIC overlap, the Type I BIC seems to disappear in the far field [Fig. 3(b)].

This phenomenon is consistent with the results observed in 1D dielectric PCs [44] but based on different principles. We observe a topological band inversion, corresponding to a transition of the geometric phase of the hybrid bands. To examine the properties of all bands, we calculated the Zak phase using [44]

$$\theta_n^{\mathrm{Zak}} = \int_{-\pi/p}^{\pi/p} dq \left[i \int_{\mathrm{unitcell}} \mathrm{d}x\mathrm{d}y u_{n,q}^*(x,y)\partial_q u_{n,q}(x,y) \right], \tag{9}$$

where $i\int_{\mathrm{unitcell}} \mathrm{d}x\mathrm{d}y u_{n,q}^*(x,y)\partial_q u_{n,q}(x,y)$ is the Berry connection and $u_{n,q}(x,y)$ is the periodic-in-cell part of the Bloch magnetic field eigenfunction of a state on the n th band with wave vector q [44]. Here, the center of the unit cell was chosen to be its inversion center located in the middle of the groove to calculate the Zak phase.

The calculated results are shown in Fig. 5. A clear Zak phase transition at the Dirac point is revealed, which confirms band inversion. Zak phases can also be determined by the symmetry of band edge states. The wave functions are always even functions of periodic direction for the band edge states at $k_{//} = \pm\pi/d$, as shown in the lower panel of (e). In (a), the Zak phase is π since the symmetry of the Bloch state at the Γ point is odd for the lower band. As the groove depth increases, the

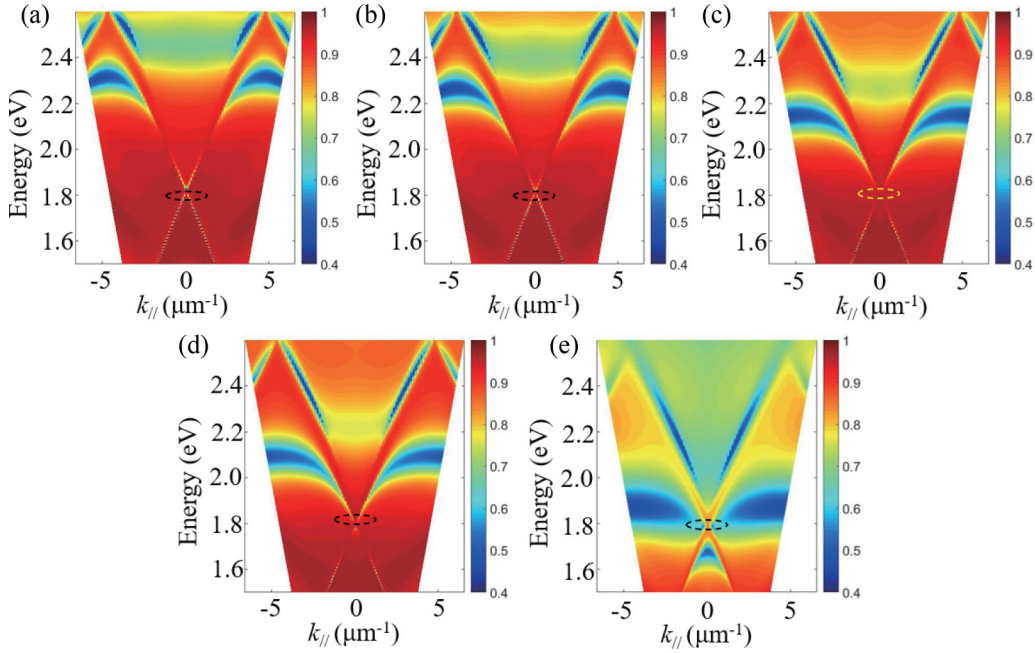

FIG. 4. Full wave simulation of the angle-resolved reflection spectra corresponding to Fig. 3. (a)–(e) The groove depth change from (a) 180 nm to (e) 270 nm. The pitch is the same as in the experiment 670 nm. The black-dashed ellipses correspond to the Type I bound states in the continuum (BICs).

band gap closes, giving rise to a Dirac point. For larger groove depths, the gap reopens, and the symmetries of the states at the Γ point are inverted, leading to a topological phase transition. Note that a Type I BIC is always in the band with $\theta_n^{\mathrm{Zak}} = \pi$. When θ_n^{Zak} cannot be determined [e.g., at the Dirac point,

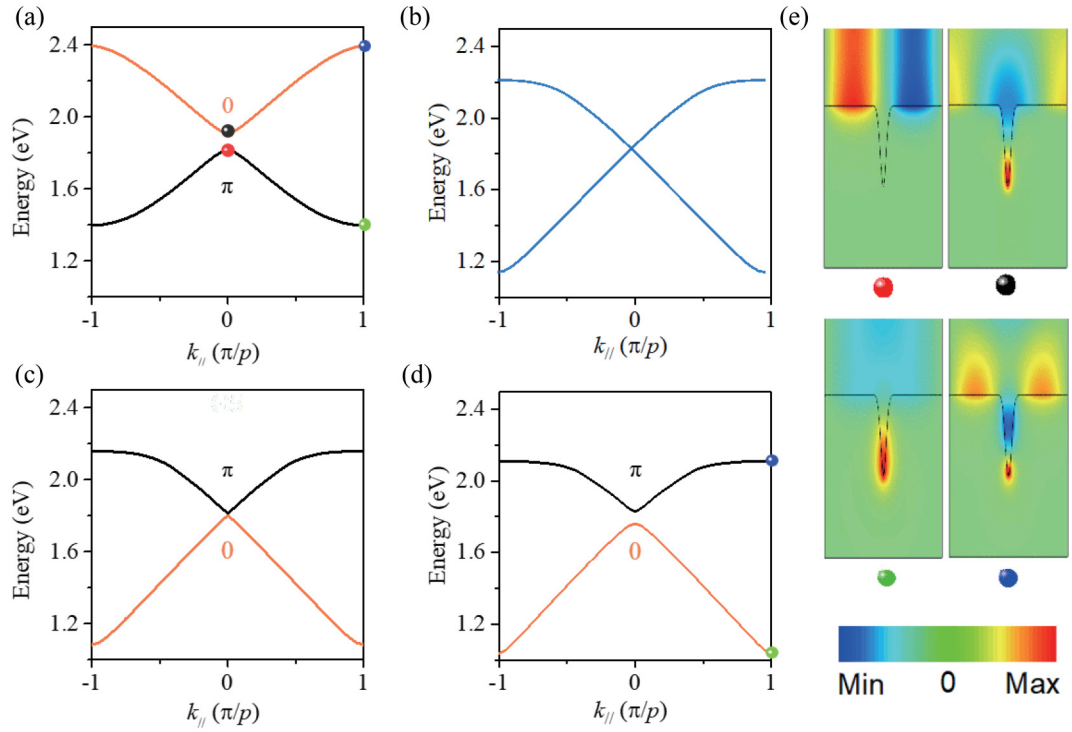

FIG. 5. Zak phase transition of the hybrid band. (a)–(d) Zak phase evolution corresponding to Figs. 3(a)–3(d). The band inversion occurs in (b), where the Zak phase cannot be defined. The center of the unit cell is chosen to be its inversion center located at the middle of the groove to calculate the Zak phase. Therefore, the Type I BIC is always in the band with $\theta_n^{\mathrm{Zak}} = \pi$. (e) The field distribution at $k_{//} = 0$ (top panel) and $k_{//} = \pm\pi/p$ (lower panel).

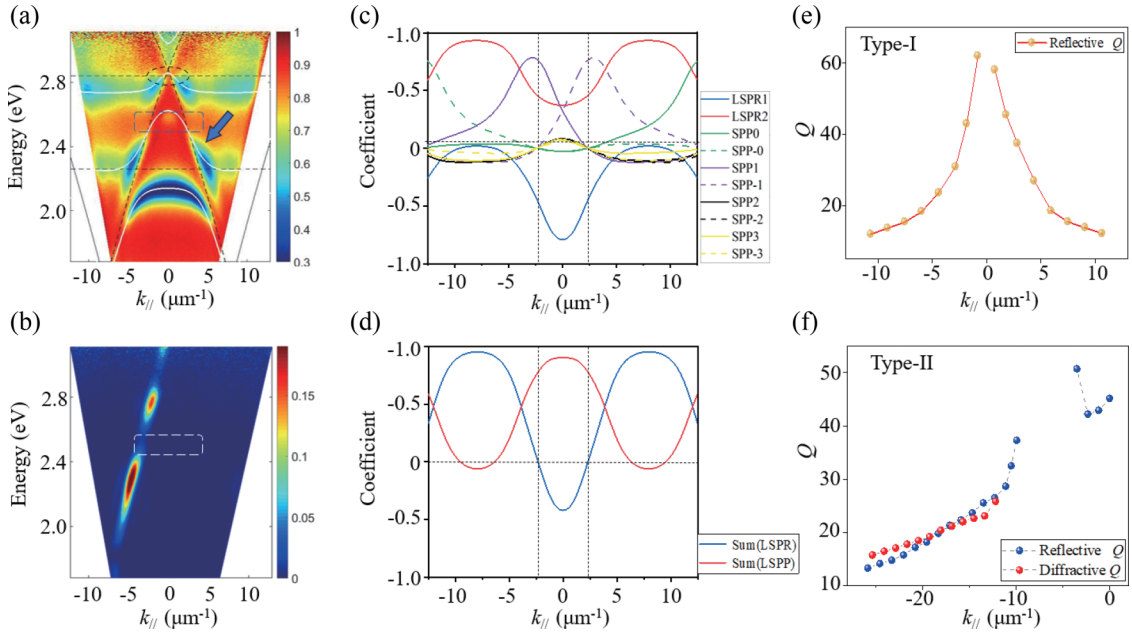

FIG. 6. Observation and characterization of Type II bound states in the continuum (BICs). (a) Angle-resolved reflection spectrum of another sample with different pitch and groove depths, showing several clear BIC features. Black-dashed ellipse: Type I BIC. Blue rectangle: Type II BIC. (b) Angle-resolved diffraction spectrum of the same sample, showing a consistent result with (a). White rectangle: Type II BIC. (c) Coefficient analysis of the band indicated by the blue arrow in (a), including both the magnitude and sign. The normalized fraction can be obtained by the square of the magnitude of the coefficient. (d) Same as (c) but a sum of the lattice surface plasmon polariton (LSPP) and localized surface plasmon resonant (LSPR) components. (e) and (f) Measured Q factors of Type I BIC (e, 62) and Type II BIC (f, 51.4) in (a) by tuning $k_{//}$.

Fig. 5(b)], the Type I BIC vanishes. This property shows that, in addition to the normal dynamic phase, the launched SPP has an extra geometric phase, even for similar band structures. This geometric phase can be modified by the LSPRs, which were determined by the groove depth and dielectric index. For example, by changing the temperature or the dielectric environment, the LSPR can be tuned across the entire visible range. This control mechanism of the SPP phase may find applications in on-chip photonic and plasmonic logic devices [45], nonlinear frequency conversion, etc.

V. FRIERICH–WINTGEN BIC

In the following section, we focus on another type of plasmonic BIC, the off-Γ-point Friedrich-Wintgen BIC. In Fig. 3, we already see that, except for Type I BICs, there are several other breakpoints at the $k_{//} \neq 0$ zone, highlighted by blue-dashed rectangles. These properties can also be found in the simulation results in Fig. 4. To confirm that these results are universal in plasmonic systems, we fabricated 10 new samples with different pitches and groove depths. A typical angle-resolved reflection spectrum of one of these samples is shown in Fig. 6(a), and the others can be found in Fig. S3 (see the Supplemental Material [46]). From these figures, we can find more BIC-like breakpoints. In addition to Type I BICs, we find at least two breakpoints at the hybrid LSPP spectra bands between any two LSPRs. We also measured angle-resolved diffraction spectra of the same samples at grazing incidence [Fig. 2(b)]. For diffraction angle-resolved spectroscopy, we replaced the objective with a dark-field objective and added a customized dark-field-blocking module behind the light source. The incident light was projected on the sample by grazing incidence (∼75 °) and blocking zero-order diffracted light (reflected light). The spectrum shown in Fig. 6(b) corresponds to Fig. 6(a), and the others can be found in Fig. S4. Because the backgroundless diffraction spectrum is not interfered with by the surface reflection of the light-collecting elements, the breakpoints have a higher contrast than those in Fig. 6(a). As will be shown later, the breakpoints marked by blue-dashed rectangles are Friedrich-Wintgen BICs, which are usually defined as Type II BICs.

To understand the formation mechanism of Type II BICs in these samples, we use the simplified model (ignoring decay)

$$H = \begin{pmatrix} E_{\mathrm{LSPR1}} & 0 & g_{\mathrm{str}} \\ 0 & E_{\mathrm{LSPR2}} & g_{\mathrm{str}} \\ g_{\mathrm{str}} & g_{\mathrm{str}} & E_{\mathrm{LSPP}} \end{pmatrix}. \tag{10}$$

The eigenvalue corresponding to Type II BIC is

$$E_m = \frac{E_{\mathrm{LSPR1}} + E_{\mathrm{LSPR2}}}{2}, \tag{11}$$

i.e., the average of the two LSPR modes. Note that this property is not universal, as shown later.

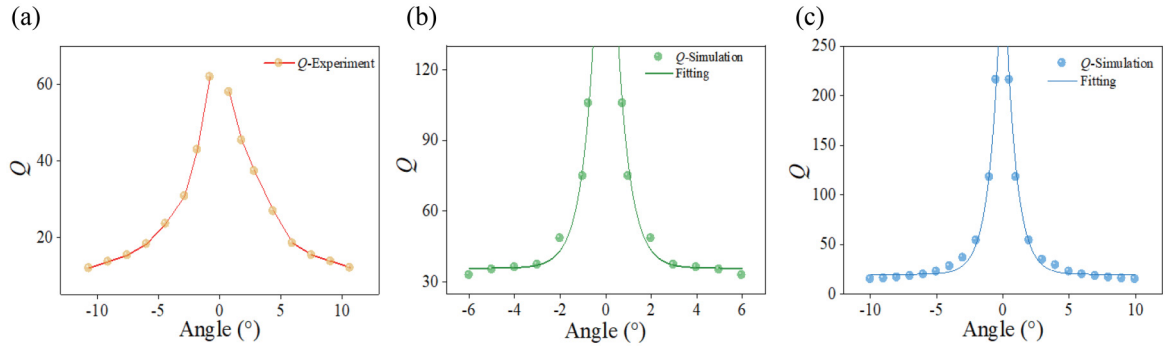

FIG. 7. The typical Q factors of Type I bound states in the continuum (BICs) extracted from experimental and simulation results. (a) Experimental results of a 10-groove sample (62). (b) Simulation results (105.8) corresponding to (a). (c) Simulation results (216) with optimized groove shape. The simulation results correspond to infinite groove numbers.

The corresponding eigenstate is

$$\psi_m = \frac{1}{\sqrt{8g_{\mathrm{str}}^2 + \Delta^2}} \begin{pmatrix} 2g_{\mathrm{str}} \\ -2g_{\mathrm{str}} \\ \Delta \end{pmatrix}, \tag{12}$$

where $\Delta = \mathrm{E_{LSPR1}} - \mathrm{E_{LSPR2}}$. From Eq. (12), we see that the two LSPR modes cancel each other.

A more rigorous analysis is shown in Figs. 6(c) and 6(d), including all the nearby LSPRs and LSPPs (10 modes). From these results, we can see that, for each hybrid band, the contributions of the original LSPR modes cancel each other out precisely at certain points in k-space ($\pm 2.32\,\mu\mathrm{m}^{-1}$ in this example), consistent with Eqs. (11) and (12). However, this model shows that the LSPP mode still exists, which seems to conflict with both experimental results and the BIC requirement that all far-field channels should disappear.

In fact, this confirms that CMT by itself is not a complete theory. By reconsidering the physical mechanism of LSPPs, we can understand and model the emergence of Type II BICs very well. When far-field light is incident on a metallic grating with nanogrooves, the LSPR can be excited, either resonant or nonresonant. The LSPRs in all grooves couple to each other to generate an LSPP. If the LSPR is resonant, then strong coupling between LSPR and LSPP will take place, as shown in the Type I BIC. If the LSPR is nonresonant, then the simple scattering by the periodic grooves is sufficient to launch the SPP but without strong coupling. However, when all the LSPR channels to the far-field cancel each other, no SPP is launched, and neither LSPR modes nor LSPP modes can be seen, resulting in the formation of a Type II BIC. According to this mechanism, these states are Friedrich-Wintgen-type BICs.

The above analysis shows that the Type II BIC can also be controlled by the LSPR with even better sensitivity, which is evident in Fig. 3. One example with deeper grooves (hence more LSPR modes) is shown in Fig. S5. Here, more Type II BICs can be found. Note that, in this case, the three nearest LSPRs should be considered together; therefore, Eq. (11) does not hold anymore.

Friedrich-Wintgen BICs are robust to small changes in the system parameters [48–50]. In our paper, Type II BICs only depend on LSPRs and are not affected by pitch. From Figs. 2–6 and Fig. S2-4, we find that both Type I and II BICs can be tuned and controlled, either by the grating pitch or groove depth. Thus, we can design and tune the two types of plasmonic BICs with full degrees of freedom.

VI. Q FACTOR OF THE BICS

Before summarizing, we discuss the Q factors of the observed plasmonic quasi-BICs. It is well known that an important feature of the BIC is the increase in Q factor associated with the reduction of radiation loss. Taking Fig. 6(a) as an example, we extracted the Q factor-angle curves of both Type I [Fig. 6(e)] and Type II [Fig. 6(f)] BICs. Clearly, they both increase when tuned close to the quasi-BICs. The measured maximal Q factor of Type I BICs is over 62, which is smaller than in simulations, as shown in Fig. 7. The reason for this result is that, as a demonstration, each sample in our sample has only 10 grooves, while in the simulations, we considered an infinite grating using periodic boundary conditions. As shown in Fig. 7(c), the simulation shows that the Q factor of Type I BIC can grow to well beyond 200 for a grating size of infinite grooves by optimizing the groove shape, thanks to the emergence of the BIC. Since plasmonic BIC is a quasi-BIC, the actual size does not need to be infinite to obtain the maximal Q factor. When the size is beyond the propagation length of SPP ($\sim$80 μm in our silver plate), ohmic loss dominates the response, and no further enhancement in Q factor can be achieved. The measured maximal Q factor of Type II BICs is 51.4. Both are much larger than the Q factor associated with the LSPR resonance ($\sim$10).

VII. CONCLUSIONS

In summary, we theoretically predicted and experimentally demonstrated that plasmonic quasi-BICs in the visible range in 1D all-metallic gratings can be observed and further controlled by strong modal coupling, despite the broad linewidth caused by metallic ohmic losses. The large Rabi splitting pushes the nearby bright mode away, uncovering the dark Type I BIC. By tuning the LSPRs, we observed a plasmonic band inversion, which corresponds to the generation of the 1D Dirac point and the "vanishing" of the BIC. This topological band inversion is characterized by the Zak phase transition. In addition, we also observe nonsymmetry-protected BICs in a 1D all-plasmonic system, the formation of which can be

understood by combining the CMT and SPP launching mechanisms. The measured Q factors of both Type I (62) and Type II (51.4) BICs are increased by one order of magnitude with only 10 grooves. The simulation results with an optimized groove shape show that, with more grooves, the Q factor can be over 200, which is 20 times larger than normal plasmonic mode in the visible range while maintaining the field confinement feature. Finally, we demonstrate that these two types of BICs can be tuned and controlled by LSPR, LSPP, or both. This additional degree of freedom makes the plasmonic system a great platform to study BIC physics and applications. For example, with the help of the BIC, the threshold of a plasmonic laser (sometimes known as spaser) can be greatly reduced. In another example, because the Q factor of BIC is much larger than that of LSPR, the temperature and refractive index sensor based on the BIC will have a much better sensitivity than the conventional plasmon sensor, which may be used as a high-sensitivity thermometer.

ACKNOWLEDGMENTS

The authors acknowledge support from the National Natural Science Foundation of China (Grants No. 91950108, No. 11774035, No. 11674032, and No. 91750102) and by the Air Force Office of Scientific Research and the Simons Foundation. We thank Che Ting Chan from the Hong Kong University of Science and Technology and Shouyong Pei and Supeng Kou from Beijing Normal University for helpful discussions.

[1] J. von Neumann and E. Wigner, Über merkwürdige diskrete Eigenwerte, Phys. Z. **30**, 465 (1929).

[2] H. Friedrich and D. Wintgen, Interfering resonances and bound states in the continuum, Phys. Rev. A **32**, 3231 (1985).

[3] C. W. Hsu, B. Zhen, A. D. Stone, J. D. Joannopoulos, and M. Soljacic, Bound states in the continuum, Nat. Rev. Mater. **1**, 16048 (2016).

[4] C. M. Linton and P. McIver, Embedded trapped modes in water waves and acoustics, Wave Motion **45**, 16 (2007).

[5] T. Lepetit and B. Kanté, Controlling multipolar radiation with symmetries for electromagnetic bound states in the continuum, Phys. Rev. B **90**, 241103(R) (2014).

[6] D. C. Marinica, A. G. Borisov, and S. V. Shabanov, Bound States in the Continuum in Photonics, Phys. Rev. Lett. **100**, 183902 (2008).

[7] E. N. Bulgakov and A. F. Sadreev, Bound states in the continuum in photonic waveguides inspired by defects, Phys. Rev. B **78**, 075105 (2008).

[8] F. Dreisow, A. Szameit, M. Heinrich, R. Keil, S. Nolte, A. Tunnermann, and S. Longhi, Adiabatic transfer of light via a continuum in optical waveguides, Opt. Lett. **34**, 2405 (2009).

[9] Y. Plotnik, O. Peleg, F. Dreisow, M. Heinrich, S. Nolte, A. Szameit, and M. Segev, Experimental Observation of Optical Bound States in the Continuum, Phys. Rev. Lett. **107**, 183901 (2011).

[10] S. Weimann, Y. Xu, R. Keil, A. E. Miroshnichenko, A. Tunnermann, S. Nolte, A. A. Sukhorukov, A. Szameit, and Y. S. Kivshar, Compact Surface Fano States Embedded in the Continuum of Waveguide Arrays, Phys. Rev. Lett. **111**, 240403 (2013).

[11] C. W. Hsu, B. Zhen, J. Lee, S. L. Chua, S. G. Johnson, J. D. Joannopoulos, and M. Soljacic, Observation of trapped light within the radiation continuum, Nature **499**, 188 (2013).

[12] F. Monticone and A. Alù, Embedded Photonic Eigenvalues in 3D Nanostructures, Phys. Rev. Lett. **112**, 213903 (2014).

[13] M. I. Molina, A. E. Miroshnichenko, and Y. S. Kivshar, Surface Bound States in the Continuum, Phys. Rev. Lett. **108**, 070401 (2012).

[14] M. Zhang and X. Zhang, Ultrasensitive optical absorption in graphene based on bound states in the continuum, Sci. Rep. **5**, 8266 (2015).

[15] Z. F. Sadrieva and A. A. Bogdanov, Bound state in the continuum in the one-dimensional photonic crystal slab, Phys. Conf. Ser. **741**, 012122 (2016).

[16] E. N. Bulgakov and A. F. Sadreev, Light trapping above the light cone in a one-dimensional array of dielectric spheres, Phys. Rev. A **92**, 023816 (2015).

[17] E. N. Bulgakov and D. N. Maksimov, Topological Bound States in the Continuum in Arrays of Dielectric Spheres, Phys. Rev. Lett. **118**, 267401 (2017).

[18] E. N. Bulgakov and A. F. Sadreev, Bound states in the continuum with high orbital angular momentum in a dielectric rod with periodically modulated permittivity, Phys. Rev. A **96**, 013841 (2017).

[19] E. N. Bulgakov and A. F. Sadreev, Scattering plane waves by a dielectric cylinder with periodically modulated permittivity at oblique incidence, Phys. Rev. A **97**, 063856 (2018).

[20] J. Lee, B. Zhen, S. L. Chua, W. Qiu, J. D. Joannopoulos, M. Soljacic, and O. Shapira, Observation and Differentiation of Unique High-Q Optical Resonances Near Zero Wave Vector in Macroscopic Photonic Crystal Slabs, Phys. Rev. Lett. **109**, 067401 (2012).

[21] H M. Doeleman,F. Monticone, W. den Hollander, A. Alu, and A. F. Koenderink, Experimental observation of a polarization vortex at an optical bound state in the continuum, Nat. Photonics, **12**, 397 (2018).

[22] H. Xu, E. J. Bjerneld, M. Kall, and L. Borjesson, Spectroscopy of Single Hemoglobin Molecules by Surface Enhanced Raman Scattering, Phys. Rev. Lett. **83**, 4357 (1999).

[23] Y. Ding, Y. You, Y. Sang, Y. Wang, M. Zhao, C. Liang, C. Lu, D. Liu, J. Zhou, Z. Tang, and J. Shi, Broadband surface-enhanced photoluminescence based on gold nanocubic self-assembly, Adv. Optical Mater. **5**, 1700551 (2017).

[24] R. F. Oulton, V. J. Sorger, T. Zentgraf, R. M. Ma, C. Gladden, L. Dai, G. Bartal, and X. Zhang, Plasmon lasers at deep subwavelength scale, Nature **461**, 629 (2009).

[25] A. Krasnok, M. Tymchenko, and A. Alù, Nonlinear metasurfaces: A paradigm shift in nonlinear optics, Mater. Today **21**, 8 (2018).

[26] S. I. Azzam, V. M. Shalaev, A. Boltasseva, and A. V. Kildishev, Formation of Bound States in the Continuum in Hybrid Plasmonic-Photonic Systems, Phys. Rev. Lett. **121**, 253901 (2018).

[27] Y. J. Chen, E. S. Koteles, R. J. Seymour, G. J. Sonek, and J. M. Ballantyne, Surface plasmons on gratings: Coupling in the minigap regions, Solid State Commun. **46**, 95 (1983).

[28] J. Fox and M. H. Schlam, *Proceedings of the Symposium on Optical and Acoustical Micro-Electronics* (Polytechnic, New York, 1975).

[29] Y. Liang, K. Koshelev, F. C. Zhang, H. Lin, S. R. Lin, J. Y. Wu, B. H. Jia, and Y. Kivshar, Bound states in the continuum in anisotropic plasmonic metasurfaces, Nano Lett. **20**, 6351 (2020).

[30] T. A. Kelf, Y. Sugawara, and J. J. Baumberg, Plasmonic Bandgaps and Trapped Plasmons on Nanostructured Metal Surfaces, Phys. Rev. Lett. **95**, 116802 (2005).

[31] R. Alexandre, J. K. Barton, B. Povazay, H. Sattman, A. Unterhuber, R. A. Leitgeb, and W. Drexler, Endoscope-tip interferometer for ultrahigh resolution frequency domain optical coherence tomography in mouse colon, Optics Express **14**, 1878 (2006).

[32] M. Meier, A. Mekis, A. Dodabalapur, A. Timko, R. E. Slusher, J. D. Joannopoulos, and O. Nalamasu, Laser action from two-dimensional distributed feedback in photonic crystals, Appl. Phys. Lett. **74**, 7 (1999).

[33] M. Imada, S. Noda, A. Chutinan, T. Tokuda, M. Murata, and G. Sasaki, Coherent two-dimensional lasing action in surface-emitting laser with triangular-lattice photonic crystal structure, Appl. Phys. Lett. **75**, 316 (1999).

[34] S. Noda, M. Yokoyama, M. Imada, A. Chutinan, and M. Mochizuki, Polarization mode control of two dimensional photonic crystal laser by unit cell structure design, Science **293**, 1123 (2001).

[35] E. Miyai, K. Sakai, T. Okano, W. Kunishi, D. Ohnishi, and S. Noda, Photonics: lasers producing tailored beams, Nature **441**, 946 (2006).

[36] H. Matsubara, S. Yoshimoto, H. Saito, J. L. Yue, Y. Tanaka, and S. Noda, GaN photonic-crystal surface emitting laser at blue-violet wavelengths, Science **319**, 445 (2008).

[37] K. Hirose, Y. Liang, Y. Kurosaka, A. Watanabe, T. Sugiyama, and S. Noda, Watt-class high-power, high-beam quality photonic-crystal lasers, Nat. Photonics **8**, 406 (2014).

[38] A. A. Yanik, A. E. Cetin, M. Huang, A. Artar, S. H. Mousavi, A. Khanikaev, J. H. Connor, G. Shvets, and H. Altug, Seeing protein monolayers with naked eye through plasmonic Fano resonances, Proc. Natl. Acad. Sci. USA **108**, 11784 (2011).

[39] B. Zhen, S. L. Chua, J. Lee, A. W. Rodriguez, X. D. Liang, S. G. Johnson, J. D. Joannopoulos, M. Soljacic, and O. Shapira, Enabling enhanced emission and low threshold lasing of organic molecules using special Fano resonances of macroscopic photonic crystals, Proc. Natl. Acad. Sci. USA **110**, 13711 (2013).

[40] J. M. Foley, S. M. Young, and J. D. Phillips, Symmetry protected mode coupling near normal incidence for narrow-band transmission filtering in a dielectric grating, Phys. Rev. B **89**, 165111 (2014).

[41] E. N. Bulgakov and A. F. Sadreev, Robust bound state in the continuum in a nonlinear microcavity embedded in a photonic crystal waveguide, Opt. Lett. **39**, 5212 (2014).

[42] H. Zheng and H. U. Baranger, Persistent Quantum Beats and Long-Distance Entanglement from Waveguide Mediated Interactions, Phys. Rev. Lett. **110**, 113601 (2013).

[43] A. F. van Loo, A. Fedorov, K. Lalumiere, B. C. Sanders, A. Blais, and A. Wallraff, Photon-mediated interactions between distant artificial atoms, Science **342**, 1494 (2013).

[44] M. Xiao, Z. Q. Zhang, and C. T. Chan, Surface Impedance and Bulk Band Geometric Phases in One-Dimensional Systems, Phys. Rev. X **4**, 021017 (2014).

[45] Y. Sang, X. J. Wu, S. S. Raja, C. Y. Wang, H. Z. Li, Y. F. Ding, D. H. Liu, J. Zhou, H. Y. Ahn, S. Gwo, and J. W. Shi, Broadband multifunctional plasmonic logic gates, Adv. Optical Mater. **6**, 1701368 (2018).

[46] See Supplemental Material at http://link.aps.org/supplemental/10.1103/PhysRevB.103.045416 for detailed analysis, fitting, and additional experimental results.

[47] C. Wang, H. Y. Chen, L. Y. Sun, W. L. Chen, Y. M. Chang, H. Ahn, X. Q. Li, and S. Gwo, Giant colloidal silver crystals for low-loss linear and nonlinear plasmonics, Nat. Commun. **6**, 7734 (2015).

[48] W. Suh, Z. Wang, and S. Fan, Temporal coupled-mode theory and the presence of non-orthogonal modes in lossless multimode cavities, IEEE J. Quantum Electron. **40**, 1511 (2004).

[49] A. Z. Devdariani, V. N. Ostrovskii, and Y. N. Sebyakin, Crossing of quasistationary levels, Sov. Phys. JETP **44**, 477 (1976).

[50] F. Monticone, H. M. Doeleman, W. Den Hollander, A. F. Koenderink, and A. Alù, Trapping light in plain sight: Embedded photonic eigenstates in zero-index metamaterials, Laser Photonics Rev. **12**, 1700220 (2018).